Available online at www.sciencedirect.com
SCIENCE DIRECT®
Journal of Computational Physics 198 (2004) 326–348
JOURNAL OF COMPUTATIONAL PHYSICS
www.elsevier.com/locate/jcp

Two-dimensional method of moments modelling of lossless overmoded transverse magnetic cavities

E. Laermans *,[1], L. Knockaert, D. De Zutter

Department of Information Technology (INTEC), Ghent University, Sint-Pietersnieuwstraat 41, B-9000 Gent, Belgium

Received 11 August 2003; received in revised form 13 January 2004; accepted 18 January 2004
Available online 20 February 2004

Abstract

We present a method of moment (MoM) analysis technique allowing to model overmoded transverse magnetic (TM) cavities in two dimensions. This technique uses the single series form of the Green's function of the empty cavity. The convergence behaviour of this series is analysed in detail.

Keywords: Method of moments; Numerical analysis; Overmoded cavities

1. Introduction

Our original idea, when we developed a method of moment (MoM) technique to model two-dimensional (2D) cavities [1], was to attempt to accurately model reverberation chambers, only relying on Maxwell's equations and not on some additional hypotheses, such as a statistical behaviour of the fields within the cavity. Little research has been performed in this non-statistical analysis – probably due to the computational complexity of the problem, especially at high frequencies – although reverberation chambers have grown more popular over the past years.

Indeed, reverberation chambers have become a classical test environment for high frequency electromagnetic compatibility (EMC) measurements [2–4] and the extension of their use for lower frequency applications has recently been studied [5,6].

The purpose of this instrument is to obtain a large, homogeneous and isotropic field within an overmoded cavity. For large structures, the exact field behaviour will strongly depend on the exact boundary conditions. The averaging of the fields is normally obtained using one or more slowly rotating stirrers. The

* Corresponding author. Tel.: +32-0(9)-2649959; fax: +32-0(9)-2649960.
E-mail addresses: eric.laermans@intec.UGent.be (E. Laermans), luc.knockaert@intec.UGent.be (L. Knockaert), daniel.dezutter@intec.UGent.be (D. De Zutter).
[1] The work of Eric Laermans is supported by a postdoctoral grant of the Fund for Scientific Research – Flanders (Belgium) (F.W.O.-Vlaanderen).

0021-9991/$ - see front matter
doi:10.1016/j.jcp.2004.01.009

fields in the chamber can then be described as statistical quantities, where each stirrer position represents a statistical sample. It is in this statistical sense that the fields can be considered approximately homogeneous and isotropic.

Besides classical mechanical stirring, the alternative of electronic mode stirring exists [7,8], where the averaging of the field distribution within the chamber is obtained using a broadband excitation signal. Some also claim the possibility of an intrinsic reverberation chamber [9], where no mechanical or electronic stirring would be required. This is more questionable as no averaging process is present in this case, contrarily to the vibrating intrinsic reverberation chamber [10–12], where the vibrating walls provide a kind of mechanical stirring.

Generally, reverberation chambers are characterised by measurements [13] or models assuming a statistical behaviour of the fields inside the chamber [14–20], possibly in combination with other methods, such as the method of moment (MoM) [21]. In [22,23] the Q-factor of a chamber is derived, starting from the assumption of statistically uniform fields within the chamber. In [24,25] the statistical information about the fields is derived from plane-wave spectrum theory.

Besides these statistical models, several – but less numerous – attempts have been made to model reverberation chambers using classic electromagnetic techniques. Three-dimensional (3D) ray-tracing [26,27] and geometrical theory of diffraction (GTD) [28] have been used at the high frequency end of the spectrum. At the lower end of the frequency spectrum – chamber dimensions smaller than 5λ – we find 3D MoM [29,30], 3D finite elements method (FEM) [31,32], 3D transmission line matrix (TLM) [33] (this method was even extended to higher frequencies in [34], where the chamber dimensions are of the order of 10λ) or even circuit models [32]. However, it is difficult to use these methods at higher frequencies as the required computer memory and computation times would increase dramatically.

The most popular modelling technique for reverberation chambers is, without contest, the finite-difference time-domain (FDTD) method [11,12,27,32,35–41]. The main advantage of this technique is that it allows to compute the full frequency response of the structure in a single run. The main drawback is probably the difficulty to cope with the high quality factor of a typical empty reverberation chamber, which would lead to unacceptably long computation times. This problem is generally circumvented by increasing the losses in the chamber – using a lossy dielectric or lossy chamber walls – which reduces the Q-factor. A first analysis of the effect of these fictitious losses on the characterisation of the chamber has been made in [42]. This convergence problem is less important for cavities loaded with a lossy object.

In order to reduce computational requirements, but still to obtain some understanding of the behaviour of reverberation chambers, some authors have restricted their analysis to a 2D approximation. This has been the case using TLM in [43], or using FEM in [44–49] for relatively low frequencies (maximal chamber dimension smaller than 10λ).

The method we present here is also a 2D approximation, but based on the MoM [1]. We consider the pure *TM* problem, with constant longitudinal line currents as excitation sources. Instead of considering the free space Green's function, we use the Green's function of the cavity. This avoids the discretisation of the cavity walls, strongly reducing the number of unknowns, which is desirable for analysis at higher frequencies. The price we have to pay is a series expression instead of a closed form for the Green's function.

We derive the integral equations for the electric field as a function of the (unknown) longitudinal currents on the conductors within the chamber. Discretising the current on the conductor boundaries and weighting the integral equations, we obtain a discrete set of equations. The expressions for the interaction and excitation integrals in this set of equations are series of analytically computed terms. Depending on the convergence behaviour of the series, they can be computed as a partial sum or using a Shanks transformation [50,51] to accelerate convergence. If these simple methods prove insufficient, we transform the series using the Veysoglu integral transform [52,53]. The criteria to choose the appropriate series calculation technique are discussed.

We validate the implementation of this method by comparing the obtained results at *low* frequencies with those obtained using CONCEPT II, a 3D MoM electromagnetic simulation tool developed at the Technische Universität Hamburg-Harburg [54]. Finally, we also show some results obtained at higher frequencies.

The first results obtained with our modelling technique were presented in [55], but they showed discrepancies with generally observed results: the computed statistical distributions of the components of the observed field did not match a normal distribution, as would be expected in a real reverberation chamber. The causes of these differences probably lie in (some of) the approximations we have made to keep our model computable: a 2D transverse magnetic (TM) model, the absence of losses and the restriction to conductor boundaries parallel with the cavity walls, zero-bandwidth, etc. In future work we hope to overcome some of these restrictions, but not all of them can be lifted easily. Introducing losses for the conductor boundaries will probably only require a minor adaptation of the model, while considering skew conductor boundaries will strongly increase the mathematical complexity of the obtained expressions. Other modifications, like introducing losses on the cavity boundaries or a 3D modelling, cannot be considered as an adaptation of the presented technique, but will require a different approach of the problem.

However, even with its limitations, our method is valuable to explore the high frequency behaviour of the fields and to examine the transition from deterministic to apparently stochastic behaviour – in fact, the behaviour remains deterministic but, due to the extreme sensitivity to changes in the geometry or the frequency, it *seems* statistical.

2. Geometry

We consider a 2D structure as shown in Fig. 1. It is invariant in the longitudinal direction – the z-direction – and has a width a and a length b. The walls of the cavity are assumed perfectly conducting. The excitation is caused by the N_e constant longitudinal line currents I_i located at $\mathbf{r}_{I,i}$ $(1 \leqslant i \leqslant N_e)$. We shall compute the currents induced on a set of N_o test objects, which are perfect conductors with boundary c_α $(1 \leqslant \alpha \leqslant N_o)$.

We impose the restriction that the boundaries of the conductors be piecewise parallel with one of the sides of the cavity, as shown in Fig. 1. This will strongly reduce the mathematical complexity of the computations.

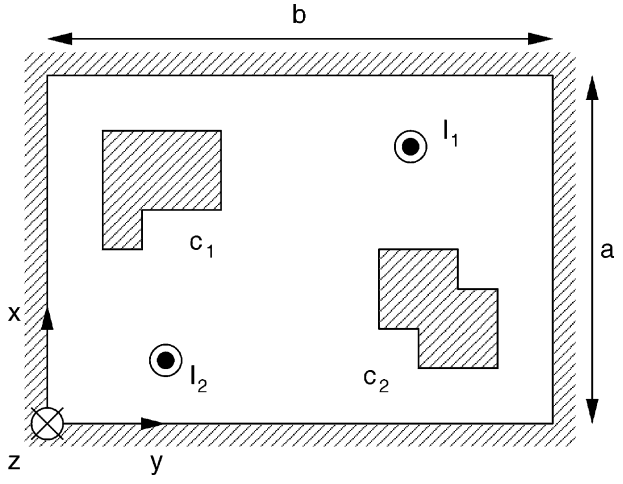

Fig. 1. Geometry of a 2D TM cavity.

3. The method

3.1. Green's function and integral equation

For the 2D structure shown in Fig. 1, the 2D Maxwell equations – fields invariant in the z-direction – reduce to the pure *TM* case:

$$\nabla_{\mathrm{tr}}^2 E_z + k^2 E_z = \mathrm{j}\omega\mu J_z, \tag{1}$$

$$\frac{\partial E_z}{\partial y} = -\mathrm{j}\omega\mu H_x, \tag{2}$$

$$\frac{\partial E_z}{\partial x} = \mathrm{j}\omega\mu H_y, \tag{3}$$

where $k = \omega\sqrt{\epsilon\mu}$ and where $\nabla_{\mathrm{tr}}^2 = (\partial^2/\partial x^2) + (\partial^2/\partial y^2)$ is the transverse Laplace operator. The longitudinal component of the magnetic field (H_z) as well as the transversal components of the electric field (E_x and E_y) are zero.

From (1) we can derive the equation for the Green's function of these *TM* equations

$$\nabla_{\mathrm{tr}}^2 G(\mathbf{r}_{\mathrm{o}}\,|\,\mathbf{r}_{\mathrm{e}}) + k^2 G(\mathbf{r}_{\mathrm{o}}\,|\,\mathbf{r}_{\mathrm{e}}) = \mathrm{j}\omega\mu\delta(\mathbf{r}_{\mathrm{o}} - \mathbf{r}_{\mathrm{e}}), \tag{4}$$

where $\mathbf{r}_{\mathrm{o}} = (x_{\mathrm{o}}, y_{\mathrm{o}})$ and $\mathbf{r}_{\mathrm{e}} = (x_{\mathrm{e}}, y_{\mathrm{e}})$ represent the coordinates of, respectively, an observation and an excitation point.

The Green's function obeying the boundary conditions of the empty cavity – $E_z = 0$ at the walls – can be written as a simple series [56] (instead of the more traditional double series):

$$G(\mathbf{r}_{\mathrm{o}}\,|\,\mathbf{r}_{\mathrm{e}}) = -\frac{\mathrm{j}\omega\mu}{a}\sum_{m=1}^{\infty}\frac{\sin\left(\frac{\pi m x_{\mathrm{o}}}{a}\right)\sin\left(\frac{\pi m x_{\mathrm{e}}}{a}\right)}{k_m^{(a)}\sin(k_m^{(a)}b)}\left\{\cos\left[k_m^{(a)}(b-(y_{\mathrm{o}}+y_{\mathrm{e}}))\right] - \cos\left[k_m^{(a)}(b-|y_{\mathrm{o}}-y_{\mathrm{e}}|)\right]\right\} \tag{5}$$

$$= -\frac{\mathrm{j}\omega\mu}{a}\sum_{m=1}^{\infty} g_m^{(a)}(\mathbf{r}_{\mathrm{o}}\,|\,\mathbf{r}_{\mathrm{e}}), \tag{6}$$

where $k_m^{(a)}$ is defined as

$$k_m^{(a)} = \sqrt{\left(\frac{\omega}{c}\right)^2 - \left(\frac{\pi m}{a}\right)^2}. \tag{7}$$

The expression $g_m^{(a)}$ can be understood as a kind of modal Green's function corresponding to the $TM_{m,*}$-modes of the 2D cavity.

From (1) and (4) we derive an expression for the longitudinal electric field E_z at an arbitrary observation point $\mathbf{r}_{\mathrm{o}}$ within the cavity as a function of the unknown current density $J_{z,\alpha}$ on the conductor boundaries c_α and of the excitation currents I_i

$$E_z(\mathbf{r}_{\mathrm{o}}) = \sum_{i=1}^{N_{\mathrm{e}}} I_i G(\mathbf{r}_{\mathrm{o}}\,|\,\mathbf{r}_{I,i}) + \sum_{\alpha=1}^{N_{\mathrm{o}}}\oint_{c_\alpha} G(\mathbf{r}_{\mathrm{o}}\,|\,\mathbf{r}_{\mathrm{e}}) J_{z,\alpha}(\mathbf{r}_{\mathrm{e}})\,\mathrm{d}c_{\mathrm{e}}, \tag{8}$$

where the first term represents the direct contribution from each line current excitation i ($1 \leqslant i \leqslant N_{\mathrm{e}}$), located at an excitation point $\mathbf{r}_{I,i}$, while the second term represents the contribution from the induced currents.

We discretise the conductor boundaries in n_{e} excitation segments and n_{o} observation segments. The current density is approximated by a pulse basis function on each excitation segment, yielding a piecewise

constant current density approximation. The electric field boundary condition ($E_z = 0$) is imposed at the N_o conductor boundaries and is weighted over each observation segment using pulse weighting functions. From this, we obtain a discrete set of equations from (8)

$$\sum_{k=1}^{n_e} Z_{jk} J_{z,k} = -\sum_{i=1}^{N_e} V_{i,j} \quad (1 \leqslant j \leqslant n_o), \tag{9}$$

where $J_{z,k}$ is the current density amplitude at excitation segment k and where the interaction (Z_{jk}) and excitation ($V_{i,j}$) matrix elements are defined as

$$Z_{jk} = \int_s w_j(s) \int_{s'} b_k(s') G(\mathbf{r}_o(s) \,|\, \mathbf{r}_e(s')) \, \mathrm{d}s' \, \mathrm{d}s, \tag{10}$$

$$V_{i,j} = I_i \int_s w_j(s) G(\mathbf{r}_o(s) \,|\, \mathbf{r}_{I,i}) \, \mathrm{d}s, \tag{11}$$

where s is a length parameter along the observation segments and s' is a length parameter along the excitation segments. We use the notation b_k for the basis function corresponding to excitation segment k, and the notation w_j for the weighting function corresponding to observation segment j. As announced before, we shall use pulse functions for both b_k and w_j. This means that b_k and w_j are equal to one on excitation segment k, respectively, on observation segment j and zero elsewhere.

It is not necessary that excitation and observation segments coincide. We may choose to consider more observation segments than excitation segments to obtain an overdetermined set of equations, which can be solved in the least-squares sense. The overdetermination of the equation set should guarantee a better numerical stability, as the system may be ill-conditioned, especially at high frequencies.

3.2. Modal integrals

In the same way as we could write the Green's function as a series of modal Green's functions (6), we can rewrite the interaction integrals (10) as a series of modal integrals

$$Z_{jk} = -\frac{\mathrm{j}\omega\mu}{a} \sum_{n=1}^{\infty} z_{jk;m}^{(a)}, \tag{12}$$

where

$$z_{jk;m}^{(a)} = \int_s w_j(s) \int_{s'} b_k(s') g_m^{(a)}(\mathbf{r}_o(s) \,|\, \mathbf{r}_e(s')) \, \mathrm{d}s' \, \mathrm{d}s. \tag{13}$$

And similarly, we can rewrite the excitation integrals (11) as the following series:

$$V_{i,j} = -\frac{\mathrm{j}\omega\mu}{a} I_i \sum_{n=1}^{\infty} v_{i,j;m}^{(a)}, \tag{14}$$

where

$$v_{i,j;m}^{(a)} = \int_s w_j(s) g_m^{(a)}(\mathbf{r}_o(s) \,|\, \mathbf{r}_{I,i}) \, \mathrm{d}s. \tag{15}$$

The modal interaction (13) and excitation (15) integrals are computed analytically. In the following, we shall focus on a particular type of modal interaction integral. More details about the computation of other modal interaction or excitation integrals can be found in Appendixes A and B of this paper.

We consider the case of a modal interaction integral where both interaction and observation segment are parallel with the x-axis. In this configuration, using the expression for $g_m^{(a)}(\mathbf{r}_o\,|\,\mathbf{r}_e)$ from (5) and (6), and performing the double integration (over the variables x' and x) from (13), we obtain after some straightforward calculation the modal interaction integral

$$\begin{aligned} z^{(a)}_{X_oX_e;m} = {} & \frac{\cos\left[k_m^{(a)}(b-(y_o+y_e))\right]-\cos\left[k_m^{(a)}(b-|y_o-y_e|)\right]}{2\left(\frac{\pi m}{a}\right)^2 k_m^{(a)}\sin[k_m^{(a)}b]} \\ & \times\left\{\cos\left(\frac{\pi m}{a}(x_{o2}-x_{e2})\right)+\cos\left(\frac{\pi m}{a}(x_{o2}+x_{e2})\right)\right. \\ & +\cos\left(\frac{\pi m}{a}(x_{o1}-x_{e1})\right)+\cos\left(\frac{\pi m}{a}(x_{o1}+x_{e1})\right) \\ & -\cos\left(\frac{\pi m}{a}(x_{o2}-x_{e1})\right)-\cos\left(\frac{\pi m}{a}(x_{o2}+x_{e1})\right) \\ & \left.-\cos\left(\frac{\pi m}{a}(x_{o1}-x_{e2})\right)-\cos\left(\frac{\pi m}{a}(x_{o1}+x_{e2})\right)\right\}, \end{aligned} \tag{16}$$

where (x_{e1},y_e) and (x_{e2},y_e), respectively, are the start and the end coordinates of the considered excitation segment, and where (x_{o1},y_o) and (x_{o2},y_o), respectively, are the start and the end coordinates of the considered observation segment.

This modal interaction integral becomes infinite if for some value m_0 of the index m, $k_{m_0}^{(a)}=n_0\pi$, where both m_0 and n_0 are non-zero. This coincides with a resonance frequency f_{m_0,n_0} of the empty cavity

$$f_{m_0,n_0}=\frac{c}{2}\sqrt{\left(\frac{m_0}{a}\right)^2+\left(\frac{n_0}{b}\right)^2}. \tag{17}$$

However, these resonance frequencies are not necessarily the resonance frequencies of the cavity in which test objects are present. Indeed, the singularity occurs in all excitation (14) and interaction (12) integrals, which means it can be removed from both the left- and the right-hand side of the set of equations (9), yielding finite solutions for the current density on the conductor boundaries. Only when the interaction matrix Z_{jk} in the left-hand side of the set of equations (9) becomes singular, will the current density J_z become unbound. This occurs at the resonance frequencies of the loaded cavity.

We should also notice that the case $k_{m_0}^{(a)}=0$ does not yield a singularity in the expression for the modal interaction integral (16), as was to be expected as no $TM_{m_0,0}$ modes exist for the empty cavity.

3.3. Series computation

For sufficiently low values of the modal order m ($m\leqslant 2fa/c$), the parameter $k_m^{(a)}$ in (16) is real and the convergence of the series is dominated by the $1/m^2$ factor, which is a very slow decay. This means that all lower order terms in the series will have to be computed explicitly.

For large values of the mode order m, the value of the parameter $k_m^{(a)}$ in (16) becomes purely imaginary. This means that for sufficiently large values of m, the terms in (16) will behave as

$$C\frac{\exp\left(-\beta\sqrt{m^2-\alpha^2}\right)}{m^2\sqrt{m^2-\alpha^2}}\cos(m\gamma), \tag{18}$$

where C is a constant factor, independent of the mode index m, and where the parameters α, β and γ will define the convergence behaviour of the series:

$$\alpha = \frac{2fa}{c}, \tag{19}$$

$$0 \leqslant \beta \leqslant 2\pi\frac{b}{a}, \tag{20}$$

$$0 \leqslant |\gamma| \leqslant 2\pi. \tag{21}$$

As long as the product $\alpha\beta$ in (18) is sufficiently large – e.g. larger than 5 – the convergence of the series is sufficient to allow direct computation.

For smaller values of $\alpha\beta$, acceleration techniques may be useful or even necessary. If the parameter γ is not too small – $|\sin\gamma| > 0.1$ – the oscillations in the series terms are sufficiently rapid to allow for an efficient use of classical series acceleration techniques, such as the Shanks transformation [50,51]. We should note that small values for $\alpha\beta$ also occur at high frequencies, for example when excitation and observation segments are near to each other.

However, when both $\alpha\beta$ and γ are small, a series as (18) will have slowly converging, slowly oscillating terms. Such a series cannot easily be computed using direct computation or classical series acceleration techniques. These techniques are known to fail on such series.

For this kind of series, we use a variant of the Veysoglu transformation described in [52,53]. This technique transforms an oscillating series into an integral expression

$$\sum_{m=1}^{\infty} \mathrm{e}^{-\mathrm{j}\gamma m} F(m) = \mathrm{e}^{-\mathrm{j}\gamma} \int_{-\infty}^{+\infty} \frac{f(u)\mathrm{e}^{-u}}{1 - \mathrm{e}^{-u}\mathrm{e}^{-\mathrm{j}\gamma}}\, \mathrm{d}u, \tag{22}$$

where $f(u)$ is the inverse Laplace transform of $F(s)$

$$f(u) = \mathscr{L}^{-1}[F(s)](u) \tag{23}$$

or

$$F(s) = \mathscr{L}[f(u)](s) = \int_{-\infty}^{+\infty} f(u)\mathrm{e}^{-su}\, \mathrm{d}u. \tag{24}$$

We can generalise the principle of this transformation to series tails (i.e. series with a start index p different from 1), taking into account that

$$\sum_{m=p}^{\infty} \mathrm{e}^{-\mathrm{j}\gamma m} F(m) = \mathrm{e}^{-\mathrm{j}\gamma(p-1)} \sum_{m=1}^{\infty} \mathrm{e}^{-\mathrm{j}\gamma m} F(m + (p-1)) \tag{25}$$

and that

$$f(u)\mathrm{e}^{-(p-1)u} = \mathscr{L}^{-1}[F(s + (p-1))](u) \tag{26}$$

we can then apply (22), which yields

$$\sum_{m=p}^{\infty} \mathrm{e}^{-\mathrm{j}\gamma m} F(m) = \mathrm{e}^{-\mathrm{j}\gamma p} \int_{-\infty}^{+\infty} \frac{f(u)\mathrm{e}^{-pu}}{1 - \mathrm{e}^{-u}\mathrm{e}^{-\mathrm{j}\gamma}}\, \mathrm{d}u. \tag{27}$$

Taking the real and imaginary parts of (27), we finally obtain

$$\sum_{m=p}^{\infty} \cos(\gamma m) F(m) = \int_{-\infty}^{+\infty} F_{\mathrm{C}}(\gamma, p, u) f(u) \mathrm{e}^{-pu}\, \mathrm{d}u, \tag{28}$$

$$\sum_{m=p}^{\infty} \sin(\gamma m) F(m) = \int_{-\infty}^{+\infty} F_{\mathrm{S}}(\gamma, p, u) f(u) \mathrm{e}^{-pu}\, \mathrm{d}u, \tag{29}$$

where the functions F_{C} and F_{S} are defined as

$$F_{\mathrm{C}}(\gamma, p, u) = \frac{\cos(\gamma p) - \cos(\gamma(p-1))\mathrm{e}^{-u}}{1 - 2\mathrm{e}^{-u}\cos\gamma + \mathrm{e}^{-2u}}, \tag{30}$$

$$F_{\mathrm{S}}(\gamma, p, u) = \frac{\sin(\gamma p) - \sin(\gamma(p-1))\mathrm{e}^{-u}}{1 - 2\mathrm{e}^{-u}\cos\gamma + \mathrm{e}^{-2u}}. \tag{31}$$

Applying this transformation on the series tail starting at index value p with the terms given in (18) yields

$$\sum_{m=p}^{\infty} \cos(m\gamma) \frac{\exp\left(-\beta\sqrt{m^2-\alpha^2}\right)}{m^2\sqrt{m^2-\alpha^2}} = \int_{\beta}^{+\infty} \mathrm{e}^{-(p-\alpha)u} F_{\mathrm{C}}(\gamma, p, u) F^{(a)}_{XX;m}(\alpha, \beta, u)\, \mathrm{d}u, \tag{32}$$

where $\mathrm{e}^{\alpha u} F^{(a)}_{XX;m}$ is the inverse Laplace transform of the non-oscillating part of (18). This function is found (for $u \geqslant \beta$) to be (cf. [57])

$$F^{(a)}_{XX;m}(\alpha, \beta, u) = \mathrm{e}^{-\alpha u} \mathscr{L}^{-1}\left[\frac{\exp\left(-\beta\sqrt{m^2-\alpha^2}\right)}{m^2\sqrt{m^2-\alpha^2}}\right](u), \tag{33}$$

$$= \mathrm{e}^{-\alpha u} \int_{\beta}^{u} (u-t) I_0\left[\alpha\sqrt{t^2-\beta^2}\right] \mathrm{d}t, \tag{34}$$

where I_0 stands for the modified Bessel function of the first kind of order zero. For values of $u < \beta$, the function is zero.

At first sight, it may seem a rather questionable progress to have transformed an ill-converging series into a double integral with a quite awkward integrand. Indeed, neither the integrand in the right-hand side of (34), neither the function F_{C}, behave in such a way to make an automatic integration easy, showing discontinuities or near-discontinuities in higher order derivatives, especially for small values of $\alpha\beta$ and γ.

This is the reason why we have chosen not to compute the inverse Laplace transform (34) directly, but rather from the following series expansion:

$$\frac{\exp\left[-\beta\sqrt{s^2-\alpha^2}\right]}{s^2\sqrt{s^2-\alpha^2}} = \frac{1}{s^2}\sum_{n=0}^{\infty} \frac{\beta^{2n}}{(2n)!}(s^2-\alpha^2)^{n-1/2} - \frac{1}{s^2}\sum_{n=0}^{\infty} \frac{\beta^{2n+1}}{(2n+1)!}(s^2-\alpha^2)^{n}. \tag{35}$$

The inverse Laplace transform of this series expansion (35) is easily obtained

$$F^{(a)}_{XX;m}(\alpha, \beta, u) = -\frac{\mathrm{e}^{-\alpha u}(\alpha u)\sin(\alpha\beta)}{\alpha^2} + \frac{1}{\alpha^2}\sum_{n=0}^{\infty}(-1)^n \frac{(\alpha\beta)^{2n}}{2^n\, n!}\left\{(\alpha u)\ \mathrm{e}^{-\alpha u}\int_0^{\alpha u} \frac{I_n(v)}{v^n}\ \mathrm{d}v - \mathrm{e}^{-\alpha u}\frac{I_{n-1}(\alpha u)}{(\alpha u)^{n-1}}\right\}$$
$$+ f^{(a)}_{XX;m}(\alpha, \beta, u, \delta, \delta', \delta^{(2)}, \ldots), \tag{36}$$

where the notation $f^{(a)}_{XX;m}(\alpha,\beta,u,\delta,\delta',\delta^{(2)},\ldots)$ stands for a sum of terms containing Dirac distributions and their derivatives. For strictly positive values of β it is obvious that this term does not contribute to the value of the integral (32) and for $\beta = 0$, this term vanishes. This is discussed in more detail in Appendix C.

This series converges rapidly for not too large values of $\alpha\beta$ – e.g. smaller than 5 – whatever the value of γ. Furthermore, it can be efficiently computed using a generalised Clenshaw's recurrence formula [58] applied on the recurrence formulas for modified Bessel functions [59]

$$I_{v-1}(z) = \frac{2v}{z} I_v(z) + I_{v+1}(z) \tag{37}$$

and for the integral expression in (36)

$$\int_0^z \frac{I_{v+1}(t)}{t^{v+1}}\,\mathrm{d}t = \frac{1}{2v+1}\left\{\int_0^z \frac{I_v(t)}{t^v}\,\mathrm{d}t - \frac{I_{v+1}(z)}{z^v}\right\}. \tag{38}$$

To be able to compute these series, we only need a sufficiently accurate implementation of the modified Bessel functions of the first kind of order zero (I_0) and of order one (I_1), as well as an implementation of the primitive function of the modified Bessel function of the first kind of order zero ($\int_0^u I_0(t)\,\mathrm{d}t$). As we only need to compute these functions for real valued arguments, these can be easily obtained or created.

Finally, the integration (32) is computed using a very simple adaptive integration scheme – no Gauss-like integration is used – allowing a nearly arbitrary precision and overcoming the not so smooth behaviour of the integrand.

3.4. CPU time requirements

Obviously, in this modelling technique, the computation of the interaction integrals will be the most time consuming part of the simulation. At sufficiently high frequencies – cavity dimensions larger than 10λ – the computation of a single series (12) is proportional to the frequency f. On the other hand, the number of interaction integrals to be computed is proportional to f^2, as the number of basis functions should be proportional to the frequency, according to a rule of thumb of at least 8–10 discretisations per wavelength. This means that the global computation time for our method is proportional to f^3.

In a traditional 2D MoM simulation, where the walls of the cavity also have to be discretised, we still have a number of basis functions proportional to the frequency. However, this number will be significantly larger than in our method, where the large cavity walls did not need to be discretised. As the computation of the interaction integrals in a traditional 2D MoM simulation is significantly easier and more rapid than in our model, the most time consuming factor of the simulation in this case is no longer necessarily the computation of the interaction integrals. The critical part of the simulation might be – at sufficiently high frequencies — the inversion of the interaction matrix, which requires a computation time proportional to f^3.

Our method will be especially advantageous to use when the objects within the cavity are small compared to the cavity dimensions. In this case, the number of unknowns required in our method will be vastly smaller than the number required in a traditional MoM simulation and the total computation time will be strongly reduced.

However, if the cavity contains (many) large objects, the number of unknowns could be reduced by less than a factor 2. If this is true, using a traditional MoM modelling technique will probably be a better choice, as the reduced number of unknowns will not outweigh the increased complexity of the computation of the interaction integrals.

4. Numerical results

4.1. Validation

We compare the results obtained at low frequencies with our modelling technique to those obtained using a commercial three-dimensional full wave electromagnetic solver, based on the MoM: CONCEPT II, developed at the Technische Universität Hamburg-Harburg [54].

The considered geometry is shown in Fig. 2. The 2D cavity is 0.707 m long by 0.5 m wide. A 1 A excitation line current source (I_1) is placed in the symmetry plane of the cavity at a distance of 0.4017 m from the left wall. The device under test (DUT) is a small square conductor (c_1) with side 1 mm and with its centre located in the same symmetry plane as the excitation line current, at a distance of 0.18 m from the left wall.

For the 3D model, we chose a 0.12 m height for the cavity. The excitation source is here replaced by a wire with radius 0.5 mm carrying a 1 A impressed current. The DUT is replaced by another wire with radius 0.5 mm. Both wires are 0.12 m long, connecting top and bottom of the 3D cavity. As the excitation current is invariant in the z-direction, this 3D configuration should be equivalent to the 2D configuration of our modelling technique. The discretisation was chosen to be sufficiently accurate up to 1 GHz (using the $\lambda/8$-rule).

Fig. 3 shows the amplitude of the current – 0 dB corresponds to 1 A – induced on the DUT for a frequency range up to 1 GHz. We used a 1MHz frequency step for the simulation with our 2D method, while for the 3D simulations, we used an adaptive frequency sampling technique [60,61], which allows an accurate simulation over a wide frequency band with a sufficiently fine resolution and a limited number of – non-equally spaced – frequency points.

Both methods yield very similar results. The maximal difference between both graphs is of the order of 1 dB. Two factors can explain this difference. First, we used a round wire with diameter 1 mm in the 3D model, while we used a square conductor with side 1 mm in the 2D model. Second, 1 dB proved to be a rather typical error margin for simulations using CONCEPT II with not too fine discretisations. We also notice a slight shift toward higher frequencies of the resonance frequencies obtained using the 3D tool.

Finally, we observe that the resonance frequencies occuring in Fig. 3 (385, 550 and 715 MHz for the lowest order modes of the loaded cavity according to our model; 387.4, 556.9 and 722.5 MHz according to the CONCEPT II simulations) differ – as we could reasonably have expected – from the resonance

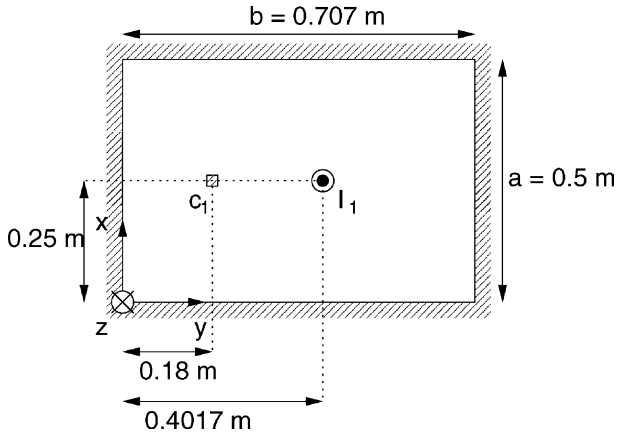

Fig. 2. Example geometry 1.

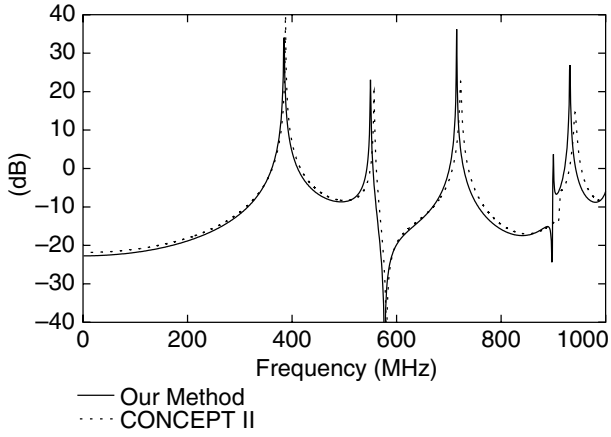

Fig. 3. Current induced on DUT (geometry 1).

frequencies of the empty cavity, which are 367.2, 519.3, 636.0 MHz, respectively, for the TM_{11}-mode, for the TM_{21}-mode and for the TM_{12}-mode. The singularity in the interaction (10) and excitation (11) integrals – due to the singularity in the Green's function (5) at these frequencies – does not have any effect on the results computed with our method.

4.2. A second example

In the second example configuration shown in Fig. 4, we again compare our results to those obtained using the 3D tool CONCEPT II at low frequencies (dimensions at the highest frequency are of the order 2λ).

The cavity is 2.718 m long by 2 m wide (and 0.5 m high in the 3D simulation). The excitation is a 1 A line current source I_1 located at 0.5 m from both left and front walls. Symmetrically placed, at the back of the cavity, is a small square conductor c_1 with side 1 mm. Another, larger, conductor c_2, with dimensions 0.12 m by 0.05 m has its centre at 0.6 m from the right wall, exactly in the middle between front and back walls of the cavity. We also compute the longitudinal electric field E_z on an observation line at a 1 m distance from the left wall, over the full width of the cavity.

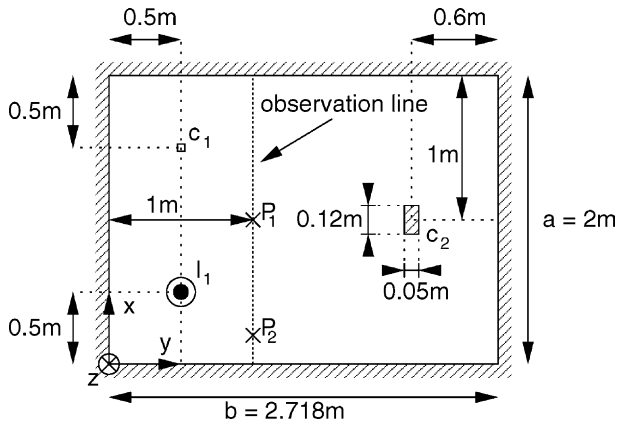

Fig. 4. Example geometry 2.

In the 3D model, we replace the excitation line current by a wire with radius 0.5 mm on which a constant 1 A current is impressed, and we replace the small square conductor by a wire with radius 0.5 mm. Both these wires and the rectangular conductor c_2 connect top and bottom of the cavity. This purely *TM* excitation of the cavity should be comparable to the 2D model.

Fig. 5 shows the amplitude of the return current – 0 dB corresponds to 1 A – on conductor c_1 according to both our model and the 3D MoM model at relatively low frequencies. Once again, the agreement between the two models is excellent, within a 1 dB error margin. As in the first example, we observe the shift toward higher frequencies of the resonance peaks in the CONCEPT II simulations.

We have also compared the results of both simulation methods for the computed longitudinal electric field E_z in two test points of the cavities. First point P_1 was located on the observation line at a distance of 0.20 m from the front wall. The second point P_2 was placed at 1 m from both front and back walls on that same observation line. The results for point P_1 and point P_2 are shown, respectively, in Figs. 6 and 7, where 0 dB corresponds to 1 V/m. Here again, the agreement between both modelling techniques is excellent, within 1 dB.

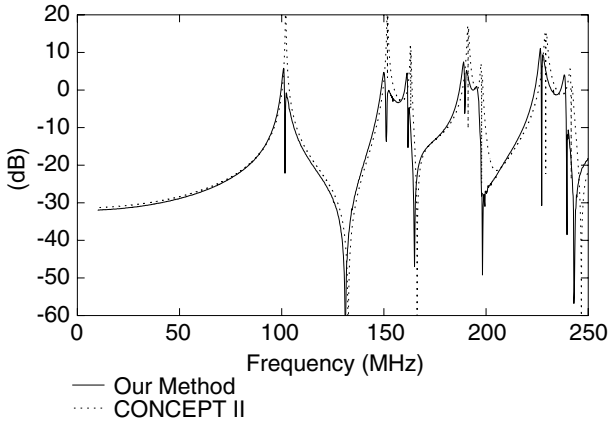

Fig. 5. Current induced on c_1 (geometry 2).

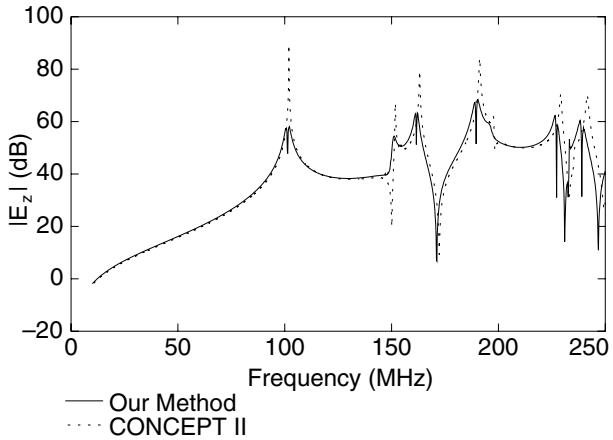

Fig. 6. Field value (geometry 2 – point P_1).

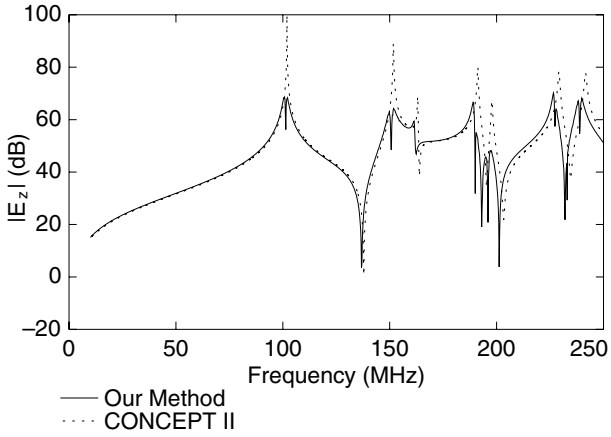

Fig. 7. Field value (geometry 2 – point P_2).

As in the first example, the resonance frequencies of the empty reverberation cavity – 93.1, 133.4 and 159.7 MHz, respectively, for the TM_{11}-mode, for the TM_{21}-mode and for the TM_{12}-mode – are not observed in the graphs for the induced currents (Fig. 5) or fields (Figs. 6 and 7), although they generate a singularity in the Green's function (5). The real resonance frequencies of the loaded cavity are observed at 101.4, 151.0 and 162.0 MHz in our model (101.9, 151.7 and 163.1 MHz in the CONCEPT II simulation).

Finally, we also show some results obtained at higher frequencies, illustrating the fact that our method is not limited to the low frequency modelling of the cavity. In Fig. 8, we show the amplitude of the induced current – 0 dB corresponds to 1 A – on both conductors c_1 and c_2 over a frequency range from 2.4 to 2.5 GHz, with a 1 MHz frequency step. At these frequencies the cavity dimensions are about 22λ by 16λ. The behaviour of the induced currents as a function of frequency becomes sensibly more complex than it was at lower frequencies (cf. Fig. 5). This is what we expected, as the number of resonance frequencies per frequency interval increases with increasing frequency. At these frequencies, a statistical description of the fields and currents in the cavity will probably be an acceptable approximation.

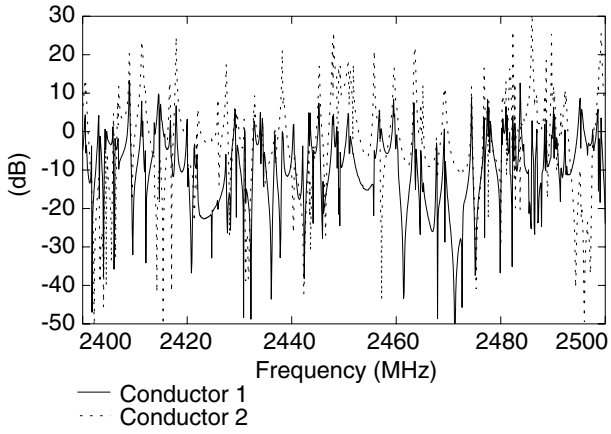

Fig. 8. Induced currents (high frequency – geometry 2).

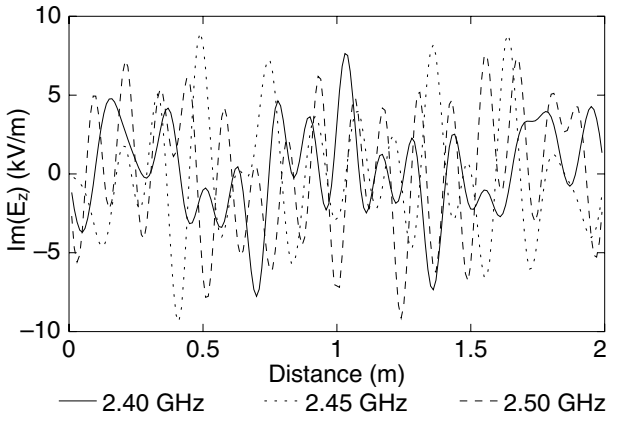

Fig. 9. Field values (high frequency – geometry 2).

We also show in Fig. 9 the behaviour of the longitudinal electric field along the observation line connecting front and back walls (cf. Fig. 4) at three discrete frequency points (2.4, 2.45 and 2.5 GHz). At these high frequencies, the field patterns are strongly dependent on the exact frequency, and the fields are only correlated over a very short range.

5. Conclusion

We have presented a two-dimensional modelling technique based on the method of moment to solve the electromagnetic problem of a large cavity. No a priori assumptions about a possible statistical behaviour of the fields and currents in the cavities are needed.

Instead of using the free space Green's function, we have considered the Green's function of the empty cavity, which allows us to avoid the explicit discretisation of the cavity walls and so to reduce the number of unknowns of the problem significantly. This will allow for a reduction of the total computation time, especially if the objects within the cavity are small compared to the cavity dimensions.

We have shown how to compute the sometimes very slowly converging series expressions for the Green's function and the resulting excitation and interaction integrals, combining straightforward computation, classical series acceleration techniques and a modified version of the Veysoglu integral transform.

At sufficiently low frequencies, the method was succesfully compared to a 3D MoM tool and the method has been shown to work for large 2D structures (over $375\lambda^2$).

Appendix A. Modal integrals

In a similar way as we computed the series terms (16), we can analytically compute the series terms of interaction and excitation integrals for other configurations of observation and excitation segments.

For the case where the excitation segment is parallel with the x-axis and the observation segment is parallel with the y-axis, we must distinguish three cases.

In the first case, where the excitation segment is lower than the observation segment ($y_e \leqslant y_{o1} < y_{o2}$), we obtain the following modal interaction integral:

$$z^{(a)}_{Y_oX_e;m} = \frac{1}{2\left(\frac{\pi m}{a}\right)\left(k^{(a)}_m\right)^2 \sin[k^{(a)}_m b]} \Big\{ \sin\Big(\frac{\pi m}{a}(x_o - x_{e2})\Big) + \sin\Big(\frac{\pi m}{a}(x_o + x_{e2})\Big) - \sin\Big(\frac{\pi m}{a}(x_o - x_{e1})\Big) - \sin\Big(\frac{\pi m}{a}(x_o + x_{e1})\Big)\Big\}\Big\{ \sin\big[k^{(a)}_m(b - (y_{o2} + y_e))\big] - \sin\big[k^{(a)}_m(b - (y_{o2} - y_e))\big] - \sin\big[k^{(a)}_m(b - (y_{o1} + y_e))\big] + \sin\big[k^{(a)}_m(b - (y_{o1} - y_e))\big]\Big\}, \tag{A.1}$$

where (x_{e1}, y_e) and (x_{e2}, y_e), respectively, are the start and the end coordinates of the considered excitation segment, and where (x_o, y_{o1}) and (x_o, y_{o2}), respectively, are the start and the end coordinates of the considered observation segment.

In the second case, where the excitation segment is higher than the observation segment ($y_{o1} < y_{o2} \leqslant y_e$), we obtain for the modal interaction integral the same expression as in (A.1), in which we should replace y_e by $b - y_e$, y_{o1} by $b - y_{o2}$, and y_{o2} by $b - y_{o1}$.

The third case is when the y-coordinate of the excitation segment lies between the y-coordinates of the start and end points of the observation segment ($y_{o1} \leqslant y_e \leqslant y_{o2}$). We then obtain the following modal interaction integral:

$$\begin{aligned} z^{(a)}_{Y_oX_e;m} = {} & \frac{1}{2\left(\frac{\pi m}{a}\right)\left(k^{(a)}_m\right)^2 \sin\left[k^{(a)}_m b\right]} \Big\{ \sin\Big(\frac{\pi m}{a}(x_o - x_{e2})\Big) + \sin\Big(\frac{\pi m}{a}(x_o + x_{e2})\Big) - \sin\Big(\frac{\pi m}{a}(x_o - x_{e1})\Big) - \sin\Big(\frac{\pi m}{a}(x_o + x_{e1})\Big)\Big\}\Big\{ \sin\big[k^{(a)}_m(b - (y_{o2} + y_e))\big] \\ & - \sin\big[k^{(a)}_m(b - (y_{o2} - y_e))\big] - \sin\big[k^{(a)}_m(b - (y_{o1} + y_e))\big] - \sin\big[k^{(a)}_m(b - (y_e - y_{o1}))\big]\Big\} \\ & + \frac{1}{\left(\frac{\pi m}{a}\right)\left(k^{(a)}_m\right)^2} \Big\{ \sin\Big(\frac{\pi m}{a}(x_o - x_{e2})\Big) + \sin\Big(\frac{\pi m}{a}(x_o + x_{e2})\Big) - \sin\Big(\frac{\pi m}{a}(x_o - x_{e1})\Big) \\ & - \sin\Big(\frac{\pi m}{a}(x_o + x_{e1})\Big)\Big\}. \end{aligned} \tag{A.2}$$

When the excitation segment is parallel with the y-axis and the observation segment is parallel with the x-axis, we obtain the same expressions as (A.1) and (A.2), in which we would have permuted the indices "e" and "o".

For a configuration where both excitation and observation segments are parallel with the y-axis, we obtain the following expression for the modal interaction integral:

$$\begin{aligned} z^{(a)}_{Y_oY_e;m} = {} & \frac{\cos\left(\frac{\pi m}{a}(x_o - x_e)\right) - \cos\left(\frac{\pi m}{a}(x_o + x_e)\right)}{2\left(k^{(a)}_m\right)^3 \sin\left[k^{(a)}_m b\right]} \big\{ - \cos\big[k^{(a)}_m(b - |y_{e2} - y_{o2}|)\big] \\ & - \cos\big[k^{(a)}_m(b - (y_{e2} + y_{o2}))\big] - \cos\big[k^{(a)}_m(b - |y_{e1} - y_{o1}|)\big] - \cos\big[k^{(a)}_m(b - (y_{e1} + y_{o1}))\big] \\ & + \cos\big[k^{(a)}_m(b - |y_{e2} - y_{o1}|)\big] + \cos\big[k^{(a)}_m(b - (y_{e2} + y_{o1}))\big] + \cos\big[k^{(a)}_m(b - |y_{e1} - y_{o2}|)\big] \\ & + \cos\big[k^{(a)}_m(b - (y_{e1} + y_{o2}))\big]\big\} - \frac{d_{\text{over}}}{\left(k^{(a)}_m\right)^2} \Big\{ \cos\Big(\frac{\pi m}{a}(x_o - x_e)\Big) - \cos\Big(\frac{\pi m}{a}(x_o + x_e)\Big)\Big\}, \end{aligned} \tag{A.3}$$

where (x_e, y_{e1}) and (x_e, y_{e2}), respectively, are the start and the end coordinates of the considered excitation segment, where (x_o, y_{o1}) and (x_o, y_{o2}), respectively, are the start and the end coordinates of the considered observation segment, and where d_{over} is the overlapping distance between the projections of excitation and observation segments on the y-axis. We can consider six different situations:

$$y_{e2} > y_{e1} \geqslant y_{o2} > y_{o1} \Rightarrow d_{over} = 0, \tag{A.4}$$
$$y_{e2} \geqslant y_{o2} > y_{o1} \geqslant y_{e1} \Rightarrow d_{over} = y_{o2} - y_{o1}, \tag{A.5}$$
$$y_{e2} \geqslant y_{o2} > y_{e1} \geqslant y_{o1} \Rightarrow d_{over} = y_{o2} - y_{e1}, \tag{A.6}$$
$$y_{o2} > y_{o1} \geqslant y_{e2} > y_{e1} \Rightarrow d_{over} = 0, \tag{A.7}$$
$$y_{o2} \geqslant y_{e2} > y_{e1} \geqslant y_{o1} \Rightarrow d_{over} = y_{e2} - y_{e1}, \tag{A.8}$$
$$y_{o2} \geqslant y_{e2} > y_{o1} \geqslant y_{e1} \Rightarrow d_{over} = y_{e2} - y_{o1}. \tag{A.9}$$

Regarding the excitation integrals, we first consider the case of an observation segment parallel with the x-axis. Using (x_e, y_e) for the coordinates of the excitation point, and (x_{o1}, y_o) and (x_{o2}, y_o) for the coordinates of the start point, respectively, the end point of the observation segment, we obtain the following expression for the excitation integral:

$$v^{(a)}_{X_o;m} = \frac{\cos\left[k^{(a)}_m(b-(y_o+y_e))\right] - \cos\left[k^{(a)}_m(b-|y_o-y_e|)\right]}{2\left(\frac{\pi m}{a}\right)k^{(a)}_m \sin\left[k^{(a)}_m b\right]} \left\{ \sin\left(\frac{\pi m}{a}(x_{o2}-x_e)\right) - \sin\left(\frac{\pi m}{a}(x_{o1}-x_e)\right) - \sin\left(\frac{\pi m}{a}(x_{o2}+x_e)\right) + \sin\left(\frac{\pi m}{a}(x_{o1}+x_e)\right)\right\}. \tag{A.10}$$

When the observation segment is parallel with the y-axis, we distinguish three cases for the computation of the modal excitation integral. We use the notation (x_o, y_{o1}) and (x_o, y_{o2}) for the coordinates of the start point, respectively, the end point of the observation segment.

The first case is when the excitation point is located above the observation segment ($y_e \geqslant y_{o2} > y_{o1}$). We then obtain

$$v^{(a)}_{Y_o;m} = \frac{\cos\left(\frac{\pi m}{a}(x_o-x_e)\right) - \cos\left(\frac{\pi m}{a}(x_o+x_e)\right)}{2\left(k^{(a)}_m\right)^2 \sin\left[k^{(a)}_m b\right]} \left\{ -\sin\left[k^{(a)}_m(b-(y_{o2}+y_e))\right] + \sin\left[k^{(a)}_m(b-(y_{o1}+y_e))\right] - \sin\left[k^{(a)}_m(b-(y_e-y_{o2}))\right] + \sin\left[k^{(a)}_m(b-(y_e-y_{o1}))\right]\right\}. \tag{A.11}$$

In a second case, we consider the configuration where the excitation point is located below the observation segment ($y_{o2} > y_{o1} \geqslant y_e$). We obtain the same expression as (A.11), but after we have replaced y_e by $b - y_e$, y_{o1} by $b - y_{o2}$, and y_{o2} by $b - y_{o1}$.

The last case is when the y-coordinate of the excitation point lies between the y-coordinates of the start and end points of the observation segment ($y_{o1} \leqslant y_e \leqslant y_{o2}$). We then obtain the following modal excitation integral:

$$v^{(a)}_{Y_o;m} = \frac{\cos\left(\frac{\pi m}{a}(x_o-x_e)\right) - \cos\left(\frac{\pi m}{a}(x_o+x_e)\right)}{2\left(k^{(a)}_m\right)^2 \sin\left[k^{(a)}_m b\right]} \left\{ -\sin\left[k^{(a)}_m(b-(y_{o2}+y_e))\right] + \sin\left[k^{(a)}_m(b-(y_{o1}+y_e))\right] + \sin\left[k^{(a)}_m(b-(y_{o2}-y_e))\right] + \sin\left[k^{(a)}_m(b-(y_e-y_{o1}))\right]\right\} - \frac{\cos\left(\frac{\pi m}{a}(x_o-x_e)\right) - \cos\left(\frac{\pi m}{a}(x_o+x_e)\right)}{\left(k^{(a)}_m\right)^2}. \tag{A.12}$$

Appendix B. Series computation

The modal interaction integrals (16) generated terms of type (18) for large values of the mode order m. We can derive similar expressions for the different kinds of interaction and excitation integrals, using the same notations as in (18).

The modal interaction integrals (A.1) will behave as

$$C\frac{\exp\left(-\beta\sqrt{m^2-\alpha^2}\right)}{m(m^2-\alpha^2)}\sin(m\gamma) \tag{B.1}$$

for high mode order values. The same behaviour will be observed for the interaction integrals (A.2).

The modal interaction integrals (A.3) will behave as

$$C\frac{\exp\left(-\beta\sqrt{m^2-\alpha^2}\right)}{(m^2-\alpha^2)^{3/2}}\cos(m\gamma) \tag{B.2}$$

with some additional terms behaving as

$$C\frac{1}{(m^2-\alpha^2)}\cos(m\gamma). \tag{B.3}$$

The high order behaviour of the modal excitation integrals (A.10) is described by

$$C\frac{\exp\left(-\beta\sqrt{m^2-\alpha^2}\right)}{m\sqrt{m^2-\alpha^2}}\sin(m\gamma). \tag{B.4}$$

For the other kinds of excitation integrals (A.11) and (A.12) we observe the following behaviour:

$$C\frac{\exp\left(-\beta\sqrt{m^2-\alpha^2}\right)}{m^2-\alpha^2}\cos(m\gamma). \tag{B.5}$$

Note that we can consider (B.3) as a variant of this expression, with $\beta = 0$.

Finally, we also observe that the modal Green's function $g_m^{(a)}$ (6) – which we need to compute if we want to calculate the field in some point of the structure using (8) – behaves for large m as

$$C\frac{\exp\left(-\beta\sqrt{m^2-\alpha^2}\right)}{\sqrt{m^2-\alpha^2}}\cos(m\gamma). \tag{B.6}$$

The convergence behaviour of the different series (B.1), (B.2), (B.4), (B.5) or (B.6) is very similar to the convergence behaviour of the already discussed series (18). We can easily compute these series by direct summation when the product $\alpha\beta$ is sufficiently large ($\alpha\beta > 5$), or using a classical Shanks transformation when γ is sufficiently large ($|\sin\gamma| > 0.1$). When both γ and $\alpha\beta$ are small, we shall use the modified Veysoglu integral transforms (28) and (29) to compute the series value.

The functions F_C and F_S still have the same meaning as in (30) and in (31). The series (B.1) can then be rewritten as

$$\sum_{m=p}^{\infty}\sin(m\gamma)\frac{\exp\left(-\beta\sqrt{m^2-\alpha^2}\right)}{m(m^2-\alpha^2)} = \int_{\beta}^{+\infty} e^{-(p-\alpha)u}F_S(\gamma,p,u)F_{YX;m}^{(a)}(\alpha,\beta,u)\,du \tag{B.7}$$

in which $F^{(a)}_{YX;m}$ is defined as

$$F^{(a)}_{YX;m}(\alpha,\beta,u) = \mathrm{e}^{-\alpha u}\frac{\cosh(\alpha(u-\beta))-1}{\alpha^2} + \frac{\beta \mathrm{e}^{-\alpha u}}{\alpha}\int_\beta^u (\cosh(\alpha(u-t))-1)\frac{I_1\left[\alpha\sqrt{t^2-\beta^2}\right]}{\sqrt{t^2-\beta^2}}\,\mathrm{d}t. \tag{B.8}$$

Similarly, the Veysoglu transform applied on (B.2) yields

$$\sum_{m=p}^{\infty}\cos(m\gamma)\frac{\exp\left(-\beta\sqrt{m^2-\alpha^2}\right)}{(m^2-\alpha^2)^{3/2}} = \int_\beta^{+\infty}\mathrm{e}^{-(p-\alpha)u}F_{\mathrm{C}}(\gamma,p,u)F^{(a)}_{YY;m}(\alpha,\beta,u)\,\mathrm{d}u, \tag{B.9}$$

where $F^{(a)}_{YY;m}$ is defined as

$$F^{(a)}_{YY;m}(\alpha,\beta,u) = \frac{\mathrm{e}^{-\alpha u}}{\alpha}\int_\beta^u \sinh(\alpha(u-t))I_0\left[\alpha\sqrt{t^2-\beta^2}\right]\mathrm{d}t. \tag{B.10}$$

For the modal interactions series (B.4), we thus obtain

$$\sum_{m=p}^{\infty}\sin(m\gamma)\frac{\exp\left(-\beta\sqrt{m^2-\alpha^2}\right)}{m\sqrt{m^2-\alpha^2}} = \int_\beta^{+\infty}\mathrm{e}^{-(p-\alpha)u}F_{\mathrm{S}}(\gamma,p,u)F^{(a)}_{X;m}(\alpha,\beta,u)\,\mathrm{d}u, \tag{B.11}$$

where the function $F^{(a)}_{X;m}$ is

$$F^{(a)}_{X;m}(\alpha,\beta,u) = \mathrm{e}^{-\alpha u}\int_\beta^u I_0\left[\alpha\sqrt{t^2-\beta^2}\right]\mathrm{d}t. \tag{B.12}$$

The series (B.5) becomes

$$\sum_{m=p}^{\infty}\cos(m\gamma)\frac{\exp\left(-\beta\sqrt{m^2-\alpha^2}\right)}{m^2-\alpha^2} = \int_\beta^{+\infty}\mathrm{e}^{-(p-\alpha)u}F_{\mathrm{C}}(\gamma,p,u)F^{(a)}_{Y;m}(\alpha,\beta,u)\,\mathrm{d}u \tag{B.13}$$

with $F^{(a)}_{Y;m}$ as a shorthand notation for

$$F^{(a)}_{Y;m}(\alpha,\beta,u) = \mathrm{e}^{-\alpha u}\int_\beta^u I_0[\alpha(u-t)]I_0\left[\alpha\sqrt{t^2-\beta^2}\right]\mathrm{d}t. \tag{B.14}$$

Finally, the series (B.6) for the Green's function terms yields

$$\sum_{m=p}^{\infty}\cos(m\gamma)\frac{\exp\left(-\beta\sqrt{m^2-\alpha^2}\right)}{\sqrt{m^2-\alpha^2}} = \int_\beta^{+\infty}\mathrm{e}^{-(p-\alpha)u}F_{\mathrm{C}}(\gamma,p,u)F^{(a)}_{m}(\alpha,\beta,u)\,\mathrm{d}u, \tag{B.15}$$

where we define $F^{(a)}_m$ as

$$F^{(a)}_m(\alpha,\beta,u) = \mathrm{e}^{-\alpha u}I_0\left[\alpha\sqrt{u^2-\beta^2}\right]. \tag{B.16}$$

As for (34), the expressions (B.8), (B.10), (B.12) or (B.14) obtained from the Veysoglu transform are not immediately useful, as their computation is not totally straightforward, with the exception of (B.16). This means that we shall apply the Laplace transform on the series expansions instead of applying it on the function itself.

Instead of the expression (B.8), we obtain from the series expansion:

$$\frac{\exp\left[-\beta\sqrt{s^2-\alpha^2}\right]}{s(s^2-\alpha^2)} = \frac{1}{s}\frac{1}{s^2-\alpha^2} - \frac{1}{s}\sum_{n=0}^{\infty}\frac{\beta^{2n+1}}{(2n+1)!}(s^2-\alpha^2)^{n-1/2} + \frac{1}{s}\sum_{n=0}^{\infty}\frac{\beta^{2n+2}}{(2n+2)!}(s^2-\alpha^2)^{n} \tag{B.17}$$

the following series expansion for $F^{(a)}_{YX;m}$:

$$F^{(a)}_{YX;m}(\alpha,\beta,u) = \frac{1}{2\alpha^2}(1-\mathrm{e}^{-\alpha u})^2 + \frac{\mathrm{e}^{-\alpha u}(1-\cos(\alpha\beta))}{\alpha^2} + \frac{1}{\alpha^2}\sum_{n=0}^{\infty}(-1)^{n+1}\frac{(\alpha\beta)^{2n+1}}{2^n(2n+1)n!}\mathrm{e}^{-\alpha u} \times \int_0^{\alpha u}\frac{I_n(v)}{v^n}\,\mathrm{d}v + f^{(a)}_{YX;m}(\alpha,\beta,u,\delta,\delta',\delta^{(2)},\ldots), \tag{B.18}$$

where – as in (36) – the notation $f^{(a)}_{YX;m}(\alpha,\beta,u,\delta,\delta',\delta^{(2)},\ldots)$ stands for a sum of terms containing Dirac distributions and their derivatives. For the same reasons as in (36), this term does not contribute to the integral (B.7).

Similarly, using in (B.9) the following series expansion:

$$\frac{\exp\left[-\beta\sqrt{s^2-\alpha^2}\right]}{(s^2-\alpha^2)^{3/2}} = \frac{1}{(s^2-\alpha^2)^{3/2}} - \beta\frac{1}{s^2-\alpha^2} + \sum_{n=0}^{\infty}\frac{\beta^{2n+2}}{(2n+2)!}(s^2-\alpha^2)^{n-1/2} - \sum_{n=0}^{\infty}\frac{\beta^{2n+3}}{(2n+3)!}(s^2-\alpha^2)^{n} \tag{B.19}$$

we obtain for $F^{(a)}_{YY;m}$ the series

$$F^{(a)}_{YY;m}(\alpha,\beta,u) = -\frac{\alpha\beta}{2\alpha^2}(1-\mathrm{e}^{-2\alpha u}) + \frac{1}{\alpha^2}\sum_{n=-1}^{\infty}(-1)^n\frac{(\alpha\beta)^{2n+2}}{2^{n+1}(2n+1)(n+1)!}\mathrm{e}^{-\alpha u}\frac{I_n(\alpha u)}{(\alpha u)^n} + f^{(a)}_{YY;m}(\alpha,\beta,u,\delta,\delta',\delta^{(2)},\ldots) \tag{B.20}$$

with the now familiar notation $f^{(a)}_{YY;m}(\alpha,\beta,u,\delta,\delta',\delta^{(2)},\ldots)$ for a term yielding no contribution to (B.9).

Applying to the modal interactions series (B.11) a similar series expansion

$$\frac{\exp\left[-\beta\sqrt{s^2-\alpha^2}\right]}{s\sqrt{s^2-\alpha^2}} = \frac{1}{s}\sum_{n=0}^{\infty}\frac{\beta^{2n}}{(2n)!}(s^2-\alpha^2)^{n-1/2} - \frac{1}{s}\sum_{n=0}^{\infty}\frac{\beta^{2n+1}}{(2n+1)!}(s^2-\alpha^2)^{n} \tag{B.21}$$

yields the following expression for $F^{(a)}_{X;m}$:

$$F^{(a)}_{X;m}(\alpha,\beta,u) = -\frac{\mathrm{e}^{-\alpha u}\sin(\alpha\beta)}{\alpha} + \frac{1}{\alpha}\sum_{n=0}^{\infty}(-1)^n\frac{(\alpha\beta)^{2n}}{2^n\,n!}\mathrm{e}^{-\alpha u}\int_0^{\alpha u}\frac{I_n(v)}{v^n}\,\mathrm{d}v + f^{(a)}_{X;m}(\alpha,\beta,u,\delta,\delta',\delta^{(2)},\ldots) \tag{B.22}$$

again with a term $f^{(a)}_{X;m}(\alpha,\beta,u,\delta,\delta',\delta^{(2)},\ldots)$ yielding no contribution to (B.11).

Finally, we apply the same method on (B.5), and with the series expansion

$$\frac{\exp\left[-\beta\sqrt{s^2-\alpha^2}\right]}{(s^2-\alpha^2)} = \frac{1}{s^2-\alpha^2} - \sum_{n=0}^{\infty}\frac{\beta^{2n+1}}{(2n+1)!}\left(s^2-\alpha^2\right)^{n-1/2} + \sum_{n=0}^{\infty}\frac{\beta^{2n+2}}{(2n+2)!}(s^2-\alpha^2)^{n} \tag{B.23}$$

we obtain a new expression for $F^{(a)}_{Y;m}$:

$$F^{(a)}_{Y;m}(\alpha,\beta,u)=\frac{(1-\mathrm{e}^{-2\alpha u})}{2\alpha}+\frac{1}{\alpha}\sum_{n=0}^{\infty}(-1)^{n+1}\frac{(\alpha\beta)^{2n+1}}{2^n(2n+1)n!}\mathrm{e}^{-\alpha u}\frac{I_n(\alpha u)}{(\alpha u)^n}+f^{(a)}_{Y;m}(\alpha,\beta,u,\delta,\delta',\delta^{(2)},\ldots). \quad \text{(B.24)}$$

What was said about the convergence behaviour of (36) could be repeated here for the series (B.18), (B.20), (B.22) and (B.24). They converge rapidly for small values of the product $\alpha\beta$ ($\alpha\beta<5$), even when the series is slowly oscillating ($|\sin\gamma|<0.1$). These series are computed in a similar way as (36), combining the recurrence formulas for modified Bessel functions (37) and (38) with the use of a generalised Clenshaw's recurrence formula [58]. For these operations, we do not need the implementation of other special functions than those we already needed for the computation of (36).

The integration (B.7), (B.9), (B.13), (B.11) or (B.15) is computed in an analogous way to (32).

Appendix C. Contribution of the Dirac distributions

In (36) – and later in the similar expressions (B.18), (B.20), (B.22) and (B.24) – we introduced a sum of terms $f^{(a)}_{XX;m}(\alpha,\beta,u,\delta,\delta',\delta^{(2)},\ldots)$ containing Dirac distributions and their derivatives. Here, we shall discuss the origin of these Dirac distributions and their contribution to the integral (32).

We know from [57] that for $u\geqslant 0$

$$\mathscr{L}^{-1}\left[(s^2-\alpha^2)^{-1/2}\right](u)=I_0(\alpha u) \quad \text{(C.1)}$$

while for $u<0$ the function is zero. This means we can rewrite (C.1) for all possible argument values u as

$$\mathscr{L}^{-1}\left[(s^2-\alpha^2)^{-1/2}\right](u)=I_0(\alpha u)H(u), \quad \text{(C.2)}$$

where $H(u)$ is the Heaviside distribution.

Taking into account that for a two-sided Laplace transform (24)

$$\mathscr{L}^{-1}\left[(s^2-\alpha^2)F(s)\right](u)=\left(\frac{\mathrm{d}^2}{\mathrm{d}u^2}-\alpha^2\right)\mathscr{L}^{-1}[F(s)](u) \quad \text{(C.3)}$$

it is possible to prove by recursion that

$$\mathscr{L}^{-1}\left[(s^2-\alpha^2)^{n-1/2}\right](u)=\frac{(-1)^n\alpha^{2n}(2n+1)!}{2^n\,n!}\frac{I_n(\alpha u)}{(\alpha u)^n}H(u)+\sum_{k=0}^{n-1}(-1)^k\delta^{(2n-2k-1)}(u)\frac{\alpha^{2k}(2n)!(n-k)!}{2^{2k}(2n-2k)!n!k!} \quad \text{(C.4)}$$

using the property of modified Bessel functions that $I_n(\alpha u)/(\alpha u)^n$ is a solution of the differential equation:

$$\frac{\mathrm{d}^2 f}{\mathrm{d}u^2}(u)+\frac{2n+1}{u}\frac{\mathrm{d}f}{\mathrm{d}u}(u)-\alpha^2 f=0 \quad \text{(C.5)}$$

and using the expression for the derivatives of modified Bessel functions

$$\frac{\mathrm{d}I_n}{\mathrm{d}u}(u)=I_{n+1}(u)+\frac{n}{u}I_n(u). \quad \text{(C.6)}$$

Similarly, we can prove by recursion that

$$\mathscr{L}^{-1}\left[(s^2-\alpha^2)^n\right](u)=\sum_{k=0}^{n}(-1)^k\delta^{(2n-2k)}(u)\frac{\alpha^{2k}(n)!}{k!(n-k)!} \tag{C.7}$$

starting from the basic inverse Laplace transform

$$\mathscr{L}^{-1}[1](u)=\delta(u) \tag{C.8}$$

and using (C.3).

The presence of an additional factor $1/s$ (in (B.17) or (B.21)) or $1/s^2$ (in (35)) merely means integrating expressions (C.4) or (C.7) once or twice.

However, the delta functions occuring in (C.4) or (C.7) do not contribute to the integral (36). If $\beta>0$ we know from the explicit expression (34) that $F^{(a)}_{XX;m}(\alpha,\beta,u)=0$ (or similar functions) for $u\leqslant\beta$. So, the net contribution of the Dirac distribution singularities at $u=0$ must vanish. For the special case $\beta=0$, the series (35) reduces to $1/s^2\sqrt{s^2-\alpha^2}$, which does not yield any Dirac distributions (or derivatives of it) in the computation of the inverse Laplace transformation.

A similar reasoning holds for the other integrals (B.18), (B.20), (B.22) or (B.24), using the respective explicit expressions (B.8), (B.10), (B.12) or (B.14).

References

[1] E. Laermans, F. Olyslager, D. De Zutter, A two-dimensional model for reverberant chambers, in: Proceedings of the 4th European Symposium on EMC, Brugge, Belgium, 2000, pp. 269–273.
[2] P. Corona, G. Latmiral, E. Pasolini, L. Piccioli, Use of a reverberating enclosure for measurements of radiated power in the microwave range, IEEE Trans. Electromagn. Compat. 18 (2) (1976) 54–59.
[3] M.O. Hatfield, Shielding effectiveness measurements using mode-stirred chambers: a comparison of two approaches, IEEE Trans. Electromagn. Compat. 30 (3) (1988) 229–238.
[4] P. Corona, J. Ladbury, G. Latmiral, Reverberation-chamber research-then and now: a review of early work and comparison with current understanding, IEEE Trans. Electromagn. Compat. 44 (1) (2002) 87–94.
[5] L.R. Arnaut, Operation of electromagnetic reverberation chambers with wave diffractors at relatively low frequencies, IEEE Trans. Electromagn. Compat. 43 (4) (2001) 637–653.
[6] L.R. Arnaut, Compound exponential distributions for undermoded reverberation chambers, IEEE Trans. Electromagn. Compat. 44 (3) (2002) 442–457.
[7] D.A. Hill, Electronic mode stirring for reverberation chambers, IEEE Trans. Electromagn. Compat. 36 (4) (1994) 294–299.
[8] Y. Huang, D.J. Edwards, A novel reverberating chamber: the source-stirred chamber, in: Proceedings of the 1992 IEEE International Symposium on EMC, 1992, pp. 120–124.
[9] F.B.J. Leferink, High field strength in a large volume: the intrinsic reverberation chamber, in: Proceedings of the 1998 IEEE International Symposium on EMC, Denver, CO, 1998, pp. 24–27.
[10] F.B.J. Leferink, J.-C. Boudenot, W. van Etten, Experimental results obtained in the vibrating intrinsic reverberation chamber, in: Proceedings of the 2000 IEEE International Symposium on EMC, Washington, DC, 2000, pp. 639–644.
[11] N.K. Kouveliotis, P.T. Trakadas, C.N. Capsalis, Examination of field uniformity in vibrating intrinsic reverberation chamber using the FDTD method, Electron. Lett. 38 (3) (2002) 109–110.
[12] N.K. Kouveliotis, P.T. Trakadas, C.N. Capsalis, FDTD calculation of quality factor of vibrating intrinsic reverberation chamber, Electron. Lett. 38 (16) (2002) 861–862.
[13] M.O. Hatfield, M.B. Slocum, Frequency characterization of reverberation chambers, in: Proceedings of the 1996 IEEE International Symposium on EMC, Santa Clara, CA, 1996, pp. 190–193.
[14] J.G. Kostas, B. Boverie, Statistical model for a mode-stirred chamber, IEEE Trans. Electromagn. Compat. 33 (4) (1991) 366–370.
[15] P. Corona, G. Ferrara, M. Migliaccio, Reverberating chambers as sources of stochastic electromagnetic fields, IEEE Trans. Electromagn. Compat. 38 (3) (1996) 348–356.
[16] P. Corona, G. Ferrara, M. Migliaccio, On the characterisation of the electromagnetic field in reverberating chambers, in: Proceedings of the 1997 Zürich EMC Symposium, Zürich, Switzerland, 1997, pp. 465–468.
[17] G.J. Freyer, T.H. Lehman, J.M. Ladbury, G.H. Koepke, M.O. Hatfield, Verification of fields applied to and EUT in a reverberation chamber using statistical theory, in: Proceedings of the 1998 IEEE International Symposium on EMC, Denver, CO, 1998, pp. 34–38.

[18] D.A. Hill, Linear dipole response in a reverberation chamber, IEEE Trans. Electromagn. Compat. 41 (4) (1999) 365–368.
[19] P. Corona, G. Ferrara, M. Migliaccio, Reverberating chamber electromagnetic field in presence of an unstirred component, IEEE Trans. Electromagn. Compat. 42 (2) (2000) 111–115.
[20] L.K. Warne, K.S.H. Lee, Some remarks on antenna response in a reverberation chamber, IEEE Trans. Electromagn. Compat. 43 (2) (2001) 239–240.
[21] T.H. Lehman, G.J. Freyer, M.O. Hatfield, J.M. Ladbury, G.H. Koepke, Verification of fields applied to an EUT in a reverberation chamber using numerical modeling, in: Proceedings of the 1998 IEEE International Symposium on EMC, Denver, CO, 1998, pp. 28–33.
[22] D.A. Hill, M.T. Ma, A.R. Ondrejka, B.F. Riddle, M.L. Crawford, R.T. Johnk, Aperture excitation of electrically large, lossy cavities, IEEE Trans. Electromagn. Compat. 36 (3) (1994) 169–177.
[23] D.A. Hill, A reflection coefficient derivation for the Q of a reverberation chamber, IEEE Trans. Electromagn. Compat. 38 (4) (1996) 591–592.
[24] D.A. Hill, Plane wave integral representation for fields in reverberation chambers, IEEE Trans. Electromagn. Compat. 40 (3) (1998) 209–217.
[25] D.A. Hill, J.M. Ladbury, Spatial-correlation functions of fields and energy density in a reverberation chamber, IEEE Trans. Electromagn. Compat. 44 (1) (2002) 95–101.
[26] D.-H. Kwon, R.J. Burkholder, P.H. Pathak, Ray analysis of electromagnetic field build-up and quality factor of electrically large shielded enclosures, IEEE Trans. Electromagn. Compat. 40 (1) (1998) 19–26.
[27] M. Hoëppe, S. Baranowski, P.N. Gineste, B. Demoulin, Use of a statistical gauge to test theoretical simulations of the field distribution in oversized electromagnetic cavities, in: Proceedings of the 4th European Symposium on EMC, Brugge, Belgium, 2000, pp. 557–561.
[28] K.R. Goldsmith, P.A. Johnson, Design, construction, computational EM modelling, and characterisation of an aircraft sized reverberation chamber and stirrer, in: Proceedings of the 17th Digital Avionics Systems Conference, Belleview, WA, 1998, pp. D55/1–D55/8.
[29] H.-J. Asander, G. Eriksson, L. Jansson, H. Akermark, Field uniformity analysis of a mode stirred reverberation chamber using high resolution computational modeling, in: Proceedings of the 2002 IEEE International Symposium on EMC, Minneapolis, MN, 2002, pp. 285–290.
[30] C. Bruns, P. Leuchtmann, R. Vahldieck, Three-dimensional method of moments simulation of a reverberation chamber in the frequency domain, in: Proceedings of the 2003 Zürich EMC Symposium, Zürich, Switzerland, 2003, pp. 229–232.
[31] M. Hoëppe, P.N. Gineste, B. Demoulin, Numerical modelling for mode-stirred reverberation chambers, in: Proceedings of the 2001 Zürich EMC Symposium, Zürich, Switzerland, 2001, pp. 635–640.
[32] C.R. Suriano, G.A. Thiele, J.R. Suriano, Low frequency behavior of a reverberation chamber with monopole antenna, in: Proceedings of the 2000 IEEE International Symposium on EMC, Washington, DC, 2000, pp. 645–650.
[33] A.J.M. Williams, A.P. Duffy, R.A. Scaramuzza, A modelling approach to determining the effective working volume of a mode-stirred chamber, in: Proceedings of the 1997 IEEE International Symposium on EMC, Austin, TX, 1997, pp. 187–192.
[34] W. Petirsch, A.J. Schwab, Investigation of the field uniformity of a mode-stirred chamber using diffusers based on acoustic theory, IEEE Trans. Electromagn. Compat. 41 (4) (1999) 445–451.
[35] S.-Y. Chung, J.-G. Rhee, H.-J. Rhee, K.-S. Lee, Field uniformity characteristics of an asymmetric structure reverberation chamber by FDTD method, in: Proceedings of the 2001 IEEE International Symposium on EMC, Montréal, Canada, 2001, pp. 429–434.
[36] M. Höijer, A.-M. Andersson, O. Lundén, M. Bäckström, Three-dimensional finite difference time domain analysis of reverberation chambers, in: Proceedings of the 4th European Symposium on EMC, Brugge, Belgium, 2000, pp. 263–268.
[37] M. Höijer, A.-M. Andersson, O. Lundén, M. Bäckström, Numerical simulations as a tool for optimizing the geometrical design of reverberation chambers, in: Proceedings of the 2000 IEEE International Symposium on EMC, Washington, DC, 2000, pp. 1–6.
[38] D. Zhang, J. Song, Impact of stirrers' position on the properties of a reverberation chamber with two stirrers, in: Proceedings of the 2000 IEEE International Symposium on EMC, Washington, DC, 2000, pp. 7–10.
[39] K. Harima, Y. Yamanaka, FDTD analysis on the effect of stirrers in a reverberation chamber, in: Proceedings of the 1999 IEEE International Symposium on EMC, Seattle, WA, 1999, pp. 260–263.
[40] L. Bai, L. Wang, B. Wang, J. Song, Reverberation chamber modeling using fdtd, in: Proceedings of the 1999 IEEE International Symposium on EMC, Seattle, WA, 1999, pp. 7–11.
[41] C. Carlsson, A. Wolfgang, P.-S. Kildal, Numerical FDTD simulations of a validation case for small antenna measurements in a reverberation chamber, in: Proceedings of the 2002 IEEE AP-S International Symposium, San Antonio, TX, 2002, pp. 482–485.
[42] F. Moglie, Finite difference, time domain analysis convergence of reverberation chambers, in: Proceedings of the 2003 Zürich EMC Symposium, Zürich, Switzerland, 2003, pp. 228–231.
[43] J. Clegg, A.C. Marvin, J.A.S. Angus, J.F. Dawson, Method for increasing the mode density in a reverberant screened room, IEE Proc. Sci. Meas. Technol. 143 (4) (1996) 216–220.

[44] C.F. Bunting, K.J. Moeller, C.J. Reddy, S.A. Scearce, Finite element analysis of reverberation chambers: a two-dimensional study at cutoff, in: Proceedings of the 1998 IEEE International Symposium on EMC, Denver, CO, 1998, pp. 208–212.
[45] C.F. Bunting, Two-dimensional finite element analysis of reverberation chambers: the inclusion of a source and additional aspects of analysis, in: Proceedings of the 1999 IEEE International Symposium on EMC, Seattle, WA, 1999, pp. 219–224.
[46] C.F. Bunting, K.J. Moeller, C.J. Reddy, S.A. Scearce, A two-dimensional finite-element analysis of reverberation chambers, IEEE Trans. Electromagn. Compat. 41 (4) (1999) 280–289.
[47] C.F. Bunting, Shielding effectiveness, statistical characterization, and the simulation of a two-dimensional reverberation chamber using finite element techniques, in: Proceedings of the 19th Digital Avionics Systems Conference, 2000, Philadelphia, PA, 2000, pp. 3A5/1–3A5/8.
[48] C.F. Bunting, Shielding effectiveness in a reverberation chamber using finite element techniques, in: Proceedings of the 2001 IEEE International Symposium on EMC, Montréal, Canada, 2001, pp. 740–745.
[49] C.F. Bunting, Statistical characterization and the simulation of a reverberation chamber using finite-element techniques, IEEE Trans. Electromagn. Compat. 44 (1) (2002) 214–221.
[50] D. Shanks, Non-linear transformations of divergent and slowly convergent sequences, J. Math. Phys. 34 (1955) 1–42.
[51] S. Singh, R. Singh, On the use of Shanks's transform to accelerate the summation of slowly converging series, IEEE Trans. Microwave Theory Tech. 39 (3) (1991) 608–610.
[52] M.E. Veysoglu, H.A. Yueh, R.T. Shin, J.A. Kong, Polarimetric passive remote sensing of periodic surfaces, J. Electromagn. Waves Appl. 5 (3) (1991) 267–280.
[53] A.W. Mathis, A.F. Peterson, A comparison of acceleration procedures for the two-dimensional periodic Green's functions, IEEE Trans. Antennas Propag. 44 (4) (1996) 567–571.
[54] T. Mader, H.D. Brüns, EFIE analysis of arbitrary metallic structures in the area of EMC, in: Proceedings of the 9th International Symposium on EMC, Zürich, Switzerland, 1991, pp. 457–461.
[55] E. Laermans, D. De Zutter, Modelled field statistics in two-dimensional reverberation chambers, in: Proceedings of the 5th European Symposium on EMC, Sorrento, Italy, 2002, pp. 41–44.
[56] P.M. Morse, H. Feshbach, Methods of Theoretical Physics, international student ed., McGraw-Hill, New York, 1953, p. 1365.
[57] G.E. Roberts, H. Kaufman, Table of Laplace Transforms, Saunders, Philadelphia and London, 1966.
[58] W.H. Press, S.A. Teukolsky, W.T. Vetterling, B.P. Flannery, Numerical Recipes in C: The Art of Scientific Computing, Advanced Mathematics, Cambridge University Press, Cambridge, UK, 1992, pp. 181–183.
[59] M. Abramowitz, I.A. Stegun, Handbook of Mathematical Functions with Formulas, Graphs and Mathematical Tables, Advanced Mathematics, Dover, New York, 1965, p. 376.
[60] J. Ureel, N. Faché, D. De Zutter, P. Lagasse, Adaptive frequency sampling of scattering parameters obtained by electromagnetic simulation, in: Proceedings of the 1994 IEEE AP-S International Symposium, Seattle, WA, 1994, pp. 1162–1165.
[61] F. Olyslager, E. Laermans, D. De Zutter, S. Criel, R. De Smedt, N. Lietaert, A. De Clercq, Numerical and experimental study of the shielding effectiveness of a metallic enclosure, IEEE Trans. Electromagn. Compat. 41 (3) (1999) 202–213.